

Cyclostationary analysis for fault detection in PV inverters

Mohammed Telidjane ^{a,b}, Benaoumeur Bakhti ^{c,*}

^a Valeo Vision, 34 Rue Saint-André, 93000 Bobigny, France

^b Alten, 65 av Edouard Vaillant, 92100 Boulogne Billancourt, France

^c Physics Department, University of Mascara, 29000, Mascara, Algeria

ARTICLE INFO

Keywords:

Photovoltaic inverters

Fault detection

Cyclostationary analysis

Transistor faults

Signal processing

ABSTRACT

Ensuring the reliability of photovoltaic (PV) inverters is crucial for the stable operation of PV systems. Traditional fault detection methods based on time-domain or frequency-domain analysis often struggle with noise and disturbances, limiting their sensitivity and effectiveness. This paper presents a novel fault detection approach utilizing cyclostationary analysis to enhance the identification of transistor faults in PV inverters. By exploiting the cyclostationary properties of the inverter voltage signal, we decompose it into periodic and residual components to extract fault signatures. The cyclic autocorrelation function (CAF) is computed for the residual signal, revealing hidden periodicities linked to fault conditions. The proposed method is validated by modeling PV panels under various conditions using the Bishop model and analyzing the impact of transistor open-circuit and short-circuit faults on inverter performance. Comparative analysis reveals that CAF exhibits superior fault sensitivity compared to conventional root mean square (RMS) metrics, making it a promising tool for early and robust fault detection. This approach contributes to improving PV system reliability and maintenance efficiency, paving the way for advanced diagnostic techniques in power electronics.

1. Introduction

Photovoltaic (PV) systems have emerged as a cornerstone of sustainable energy generation [1,2]. However, their efficiency and reliability can be compromised by various factors, including environmental conditions and component failures [3–5]. Among these components, power electronic inverters play a crucial role in converting DC power generated by PV panels into AC power suitable for grid integration. Ensuring the reliable operation of these inverters is essential for the overall performance and stability of PV systems.

Fault detection in photovoltaic (PV) inverters is a critical area of research [6–8], as undetected faults can lead to reduced efficiency, increased harmonic distortion, and potential system failures [9,10]. Various methods have been proposed to diagnose faults, particularly open-circuit (OC) faults in power semiconductor switches such as IGBTs. These methods can be broadly classified into conventional temporal analysis, model-based, signal processing-based, and knowledge-based approaches.

Traditional temporal analysis techniques [11], such as Fourier Transform (FT) and Short-Time Fourier Transform (STFT) [12,13], have been widely used for fault detection in power electronics systems. While effective for stationary signals, these methods struggle with nonlinear and non-stationary signals [14], which are common in PV inverters due to load variations, switching operations, and other dynamic factors.

The Fourier Transform assumes stationarity, leading to inaccurate fault detection in real-world conditions where frequency content changes over time. STFT improves upon this by providing a time-frequency representation, but its fixed resolution limits accuracy in detecting faults in rapidly changing environments.

Signal processing-based methods analyze electrical signals, such as current and voltage waveforms, to extract fault features. Techniques such as Fast Fourier Transform (FFT), STFT, and wavelet transform [15] have been applied to detect OC faults by identifying anomalies in the signal's frequency or time-domain characteristics. However, these methods still face challenges in capturing the time-varying nature of power electronics signals.

Model-based methods [16], such as sliding mode observers and interval observers, use mathematical models of the system to generate residuals that indicate faults. While these methods can provide accurate fault detection, their performance is highly dependent on the accuracy of the system model and can be sensitive to parameter variations and noise.

Knowledge-based approaches leverage historical data and machine learning techniques for fault detection [17,18]. Methods such as Principal Component Analysis (PCA) [19], Artificial Neural Networks (ANNs) [20,21], and Support Vector Machines (SVMs) [22] have been used

* Corresponding author.

E-mail addresses: telidjanemohamed@yahoo.fr (M. Telidjane), bbakhti@uni-osnabrueck.de, benaoumeur.bakhti@univ-mascara.dz (B. Bakhti).

to classify fault conditions based on training data. While effective for complex and nonlinear systems, these techniques require large, high-quality datasets and extensive training, which may not always be available in real-world applications.

Given the limitations of conventional methods, we aim in this paper to explore advanced techniques such as cyclostationary analysis [23], which is particularly suited for periodic or quasi-periodic signals like those in PV inverters. Cyclostationary signals exhibit statistical properties that vary periodically, allowing for more accurate fault detection. This approach has demonstrated superior performance in detecting faults in rotating machinery [24], as it effectively captures the cyclic nature of electronic signals. Studies have shown that cyclostationary analysis can enhance fault detection accuracy and robustness, outperforming traditional methods in many cases.

Building upon these advancements, this paper proposes a novel fault detection method for PV inverters based on cyclostationary techniques. Specifically, we apply cyclostationary analysis to the voltage signal of a PV inverter to detect transistor faults. Cyclostationarity offers a sophisticated analytical approach that is increasingly vital in the optimization and fault diagnosis of photovoltaic (PV) inverters [25,26]. By decomposing the voltage signal into periodic and residual components, it is possible to extract characteristic features associated with different fault conditions. The objective of this study is to demonstrate the effectiveness of cyclostationary analysis in fault detection and compare its performance with traditional temporal analysis methods.

The subsequent sections of this paper delve into the modeling of PV panels and the inverter system, followed by a detailed exploration of cyclostationary signal analysis and its application to fault detection. The impact of transistor faults on the cyclostationary properties of the inverter voltage signal is investigated, and the results are compared with traditional fault detection methods.

2. PV panel modeling

2.1. Sinusoidal pulse width modulation

Sinusoidal Pulse Width Modulation (SPWM) [27,28] is the most commonly used method to generate pure sinusoidal AC voltage from DC voltage. It is widely used in pure sine wave inverters. These inverters receive a fixed DC input voltage and produce a regulated AC output voltage by carefully varying the inverter's on and off times.

In SPWM, a train of pulses is generated for each gating signal by comparing a sinusoidal reference signal (frequency f_r , amplitude A_r) with a triangular carrier signal (frequency f_c , amplitude A_c). The pulse width is proportional to the amplitude of the reference signal at its center. The root-mean-square (rms) output voltage is controlled by the modulation index $M = A_r/A_c$. Increasing M increases both pulse width and output voltage. The output frequency equals the reference signal frequency, and the number of generated gating pulses is $N = f_p/2f_r$.

Fig. 1 illustrates the SPWM modulation process. A reference sinusoidal waveform is generated at the start of each cycle. This is compared with a higher-frequency triangular carrier waveform. The control pulse is set to one when the reference waveform amplitude exceeds the carrier waveform amplitude, and zero otherwise. This process is repeated for each carrier waveform cycle. The pulse width is modulated according to the instantaneous reference waveform amplitude, resulting in wider pulses for higher amplitudes and narrower pulses for lower amplitudes. The modulated pulses are applied to the inverter switch gate terminals, controlling their on and off states. By adjusting pulse widths based on the reference sinusoidal waveform, the inverter generates an AC output voltage that closely approximates the desired sinusoidal waveform.

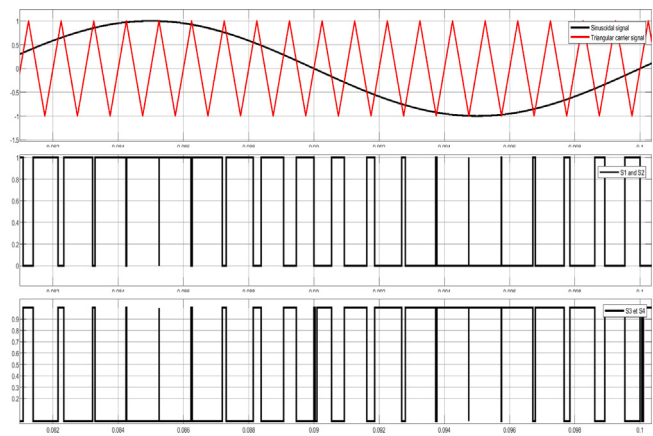


Fig. 1. SPWM generated control pulses for inverter switches.

2.2. Full H-bridge inverter design

A full H-bridge inverter is employed to reverse load current by inverting the DC voltage across the load terminals [29]. When switches S_1 and S_4 are closed, current flows through the load in one direction. Conversely, closing switches S_2 and S_3 reverses the voltage and current direction. While alternating these switch states with equal on and off times produces a square wave, the output waveform can be controlled by adjusting the duty cycle, $D = T_{on}/(T_{on} + T_{off})$, where T_{on} and T_{off} are respectively the on and off time of the switches (or pulses) and they are related to the cycle periodic time by $T = T_{on} + T_{off}$. Generating AC voltages necessitates high-speed switching, achievable with Insulated Gate Bipolar Transistors (IGBTs) to prevent short circuits. A typical switching frequency for medium-power inverters is 20 kHz, with a corresponding period of 50 ms. **Fig. 2** presents the inverter model schematic. The power stage, composed of MOSFETs or IGBTs, forms the core of the inverter. The H-bridge topology enables bidirectional current flow through upper and lower bridge sections. Each bridge consists of four switches. Switches S_1 and S_3 in the upper bridge, and S_2 and S_4 in the lower bridge, connect to the positive and negative DC input, respectively. PWM signals, generated by the control circuitry, regulate switch operation. A microcontroller or specialized PWM generator produces these signals based on the desired output waveform. Gate drivers amplify these signals to control the switches. The DC power source, such as a battery or DC power supply, provides the inverter's input voltage. The output terminals deliver the converted AC voltage. Protection components like diodes, capacitors, and snubber circuits enhance the inverter's reliability and safety.

Fig. 3 illustrates the SPWM circuit. It generates modulated pulses resembling a sinusoidal waveform for efficient DC-to-AC power conversion. A comparator compares a high-frequency carrier waveform with a reference sinusoidal waveform representing the desired output voltage. The latter is typically produced by a waveform generating circuit or voltage-controlled oscillator (VCO). A separate oscillator generates the triangular carrier waveform. The comparator's output, determined by the relative amplitudes of the reference and carrier waveforms, controls the inverter switches. These modulated pulses adjust the switch on-time to shape the output voltage into a close approximation of the desired sinusoidal waveform (see **Fig. 4**).

2.3. Simulation model

To determine the I-V characteristic of a PV cell, the Bishop model [30] was selected due to its accurate representation of experimental curves under shading conditions. This model incorporates the one-diode model and an additional term to describe the reverse bias region

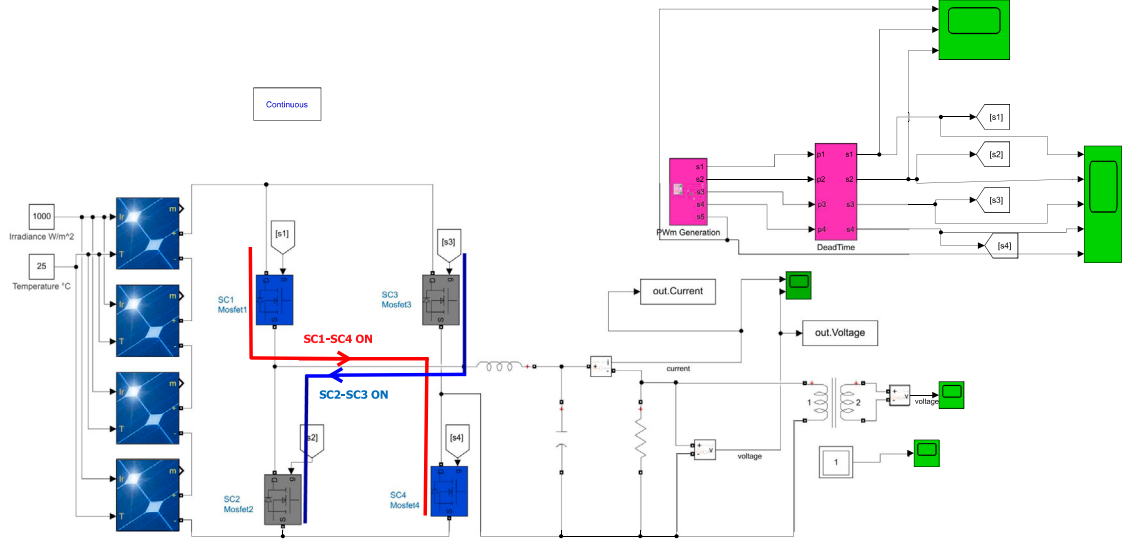


Fig. 2. Inverter model.

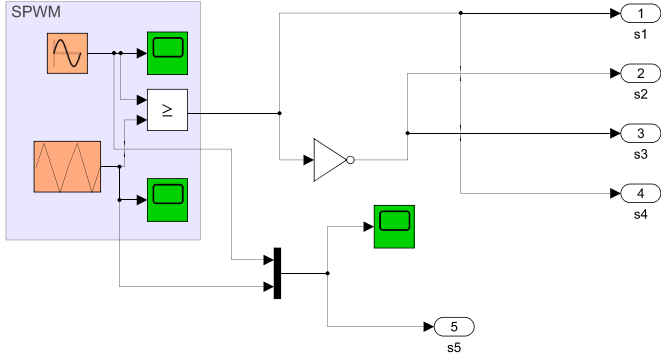


Fig. 3. SPWM model.

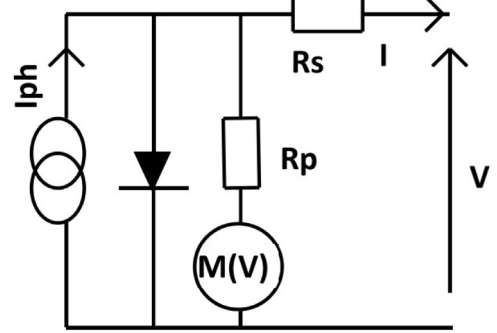


Fig. 5. Bishop model.

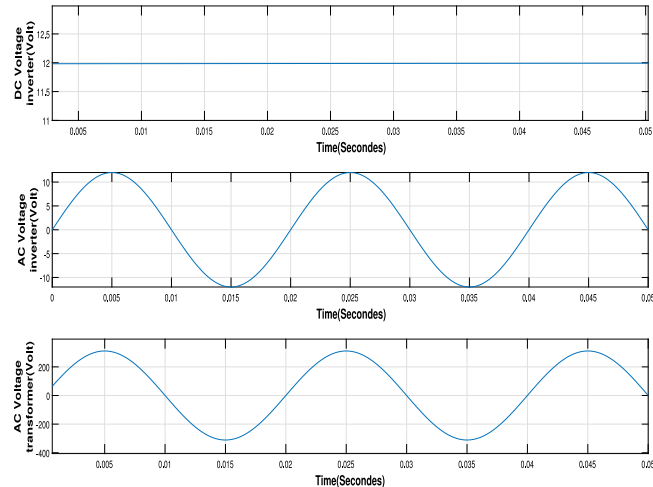


Fig. 4. 12 V to 12 V AC voltage inverter, 12 V AC to 220 V (rms) AC voltage transformer.

of the I-V curve (Fig. 5). Crucial parameters for hot spot risk assessment include the breakdown voltage V_b , shunt resistance R_p , and avalanche exponent n . To determine the current I for a given voltage V , the

Bishop equation Eq. (1) is employed.

$$I = I_{PH} - I_0 \left[\exp \left(\frac{q}{A \cdot K \cdot T} (V + R_S \cdot I) \right) - 1 \right] - \frac{V + R_S \cdot I}{R_p} M(V) \quad (1)$$

with

$$M(V) = 1 + a \left(1 - \frac{V + R_S I}{V_b} \right)^{-n} \quad (2)$$

However, due to the non-linearity introduced by the avalanche breakdown term, the Eq. (1) is reformulated into the form of Eq. (3) to apply the Newton-Raphson method for solving for I [31].

$$\begin{cases} f(I, V) = 0 \\ I_{n+1} = I_n - \frac{f(V, I_n)}{\partial f(V, I_n) / \partial I} \end{cases} \quad (3)$$

The iterative process terminates when the absolute difference between successive current values, $|I_{n+1} - I_n| < \epsilon$, falls below a specified tolerance, set at $\epsilon = 1.e - 8$ for our simulations. Once the current I is determined for a given voltage V , the algorithm is iterated to reconstruct the entire I-V curve. The PV panel parameters used in our simulation are summarized in Tab. 1. As a reference, generating an I-V curve with 600 data points takes approximately 17 ms on an Intel Core i5 – 3380M@2.90 GHz processor. When a cell is shaded, its produced voltage deviates from that of an unshaded cell at the same current. Figs. 6 compares the I-V curves of fully irradiated and 50% shaded cells, respectively. The short-circuit current is reduced by half when

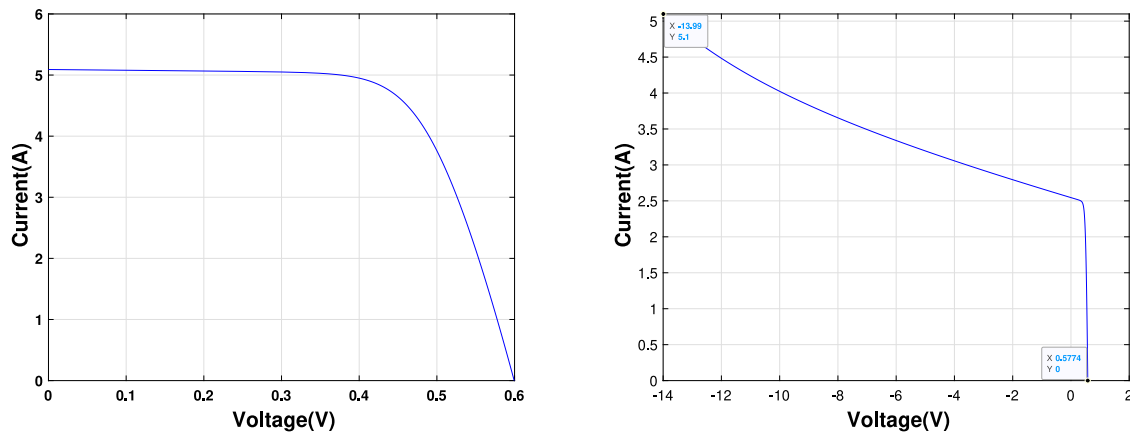


Fig. 6. PV Cell without shading (left) and with shading at 50% (right).

Table 1
Parameters of PV panel [32].

| Parameters | Values |
|-------------------------|--------|
| Number of cells | 72 |
| Number of bypass diodes | 4 |
| I_{ph} (A) | 5.1 |
| V_{oc} (V) | 43.2 |
| T_c (°K) | 298 |
| R_s (Ω) | 0.015 |
| R_p (Ω) | 9 |
| a | 1.22 |
| I_0 (A) | 2.3e-8 |

irradiance decreases by 50%. The short-circuit current of the normal cell is approximately 5 A, while that of the shaded cell is reduced to 2.5 A, demonstrating a direct correlation between short-circuit current and irradiance levels.

2.4. Role of bypass diode

When a PV cell is shaded, it can force the connected cell group into a negative operating region (Fig. 7), causing energy consumption rather than production and potentially leading to hot spots. Ideally, each PV cell would have a bypass diode to mitigate this issue. However, such a configuration is impractical due to cost and complexity. Instead, bypass diodes are typically connected in reverse parallel with groups of 18 or 24 cells, as recommended by manufacturers [33]. These diodes exhibit high resistance when the cell group is forward-biased but conduct current when the group is reverse-biased and the voltage exceeds the diode's threshold of approximately -0.6 V [34]. The overall group voltage is determined by combining the voltages of the PV cells and the bypass diode through interpolation. Fig. 8 presents the I-V characteristics of both a non-defective cell group and a defective group consisting of one shaded cell and 17 unshaded cells connected in series. We observe that a single occluded cell forces the entire group to operate in the negative region. The currents and voltages of these groups are determined by the following equations:

$$\begin{cases} I_{group,j} = I_{bypassDiode} + I_{cell} \\ V_{group,j} = \sum_{i=1}^{N_{cell}} V_{cell,i} & \text{if } \sum_{i=1}^{N_{cell}} V_{cell,i} \geq 0 \\ V_{group,j} = 0 & \text{if } \sum_{i=1}^{N_{cell}} V_{cell,i} < 0 \end{cases} \quad (4)$$

2.5. I-V characteristic of PV panel

Fig. 9 illustrates the I-V characteristic of a defective panel composed of a defective group and a non-defective group. The shading effect is evident in the deformed curve with a distinct peak. The panel's currents

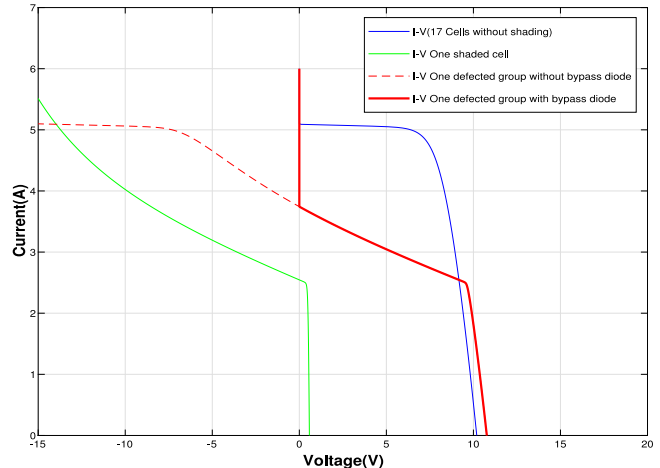


Fig. 7. I-V characteristics of one group with and without bypass diode.

and voltages, used to generate the I-V characteristic, are calculated using the following equations:

$$\begin{cases} I_{panel,k} = I_{group} \\ V_{panel,k} = \sum_{j=1}^{N_{group}} V_{group,j} \end{cases} \quad (5)$$

3. Influence of temperature and irradiance

Solar panel performance is significantly influenced by weather conditions, particularly solar irradiance and temperature [35,36]. This study employs MATLAB simulations to generate I-V and P-V curves of a photovoltaic panel under varying conditions using the parameters outlined in Table 1. The results are depicted in Figs. 10. The left panel of Fig. 10 presents the I-V characteristic of the PV panel at a constant temperature of 25 °C and different irradiance levels. A direct correlation between irradiance and both open-circuit voltage and short-circuit current is evident. The right panel of Fig. 10 displays the P-V characteristics of a PV panel maintained at a constant temperature of 25 °C under varying irradiance conditions. As irradiance increases, both the PV panel's output voltage and power output rise accordingly.

The left panel of Fig. 11 depicts the I-V characteristics for a constant irradiance of 1000 W/m² at varying temperatures. The open-circuit voltage decreases as temperature rises, while the short-circuit current exhibits a slight increase. Overall, temperature has a negative impact on open-circuit voltage. The right panel of Fig. 11 illustrates the P-V characteristics of a solar panel across a temperature range of 25 °C

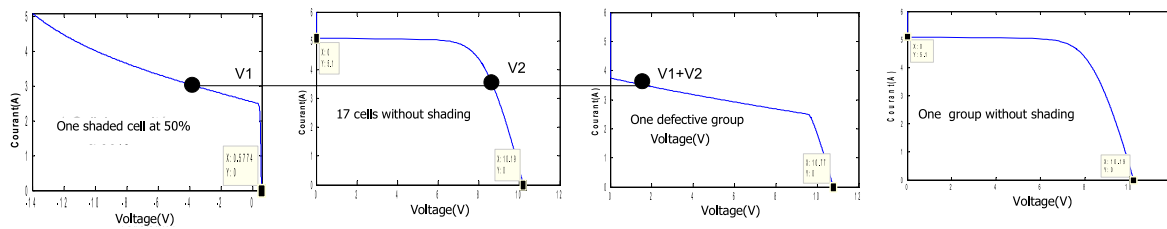


Fig. 8. I-V characteristic of non-defective group and a defective group.

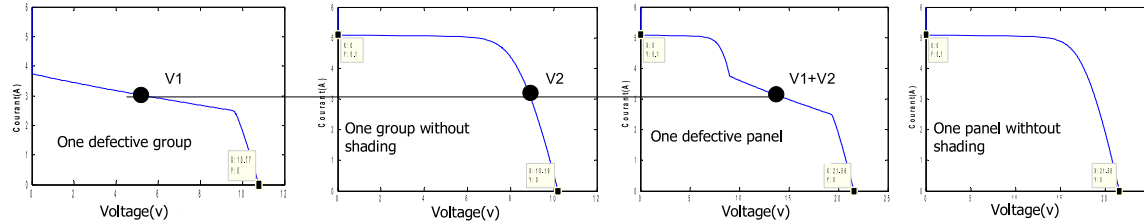


Fig. 9. I-V characteristic of non-defective panel and a defective panel.

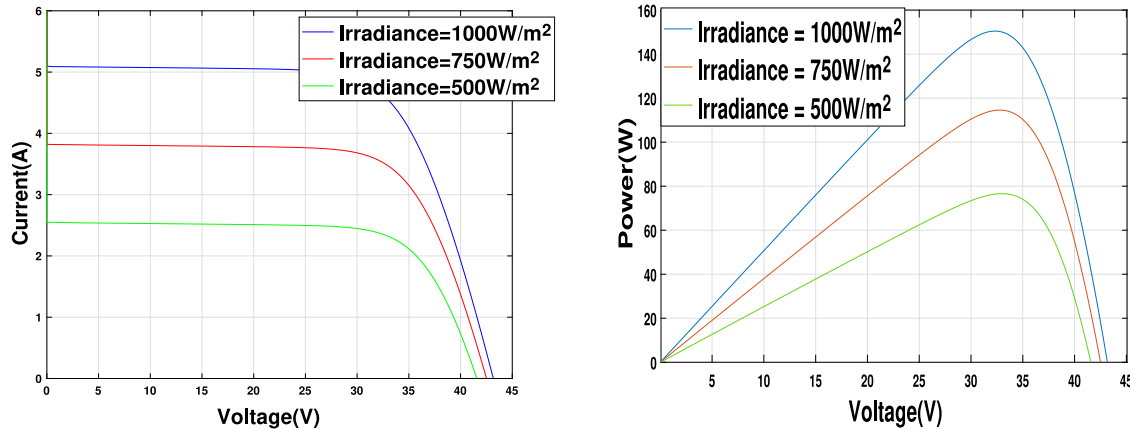


Fig. 10. I-V and P-V characteristics of PV panel for different irradiances.

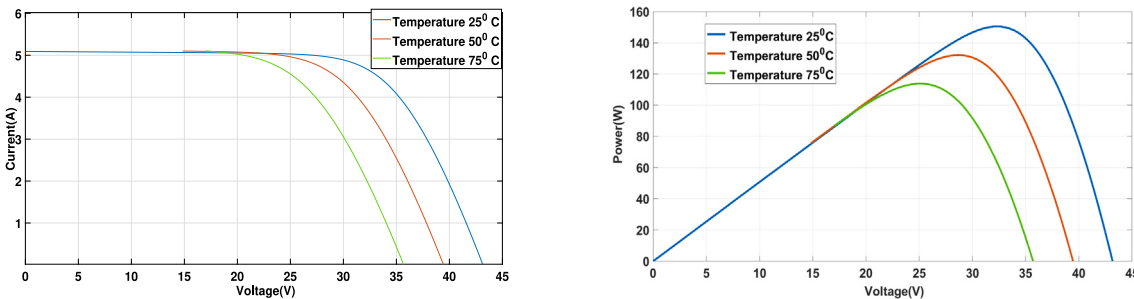


Fig. 11. I-V and P-V characteristics of PV panel for different temperatures.

to 75 °C. A clear trend emerges: as cell temperature increases, the maximum power output of the solar panel declines.

We have analyzed the modeling of PV panels, and in the next section, we explore the cyclostationary analysis of inverter voltage signals.

4. Cyclostationary signal analysis

4.1. Cyclostationarity

A signal $X(t)$ is considered first-order cyclostationary if its first-order statistical moment is periodic with period T_0 . This first-order

moment is the mean, defined as $E\{X(t + T_0)\} = E\{X(t)\}$. In practical applications with sampled signals, this quantity can be estimated using the time-synchronous average (TSA),

$$\hat{m}_x^T(t) = \frac{1}{N} \sum_{k=0}^{N-1} x(t + k.T_0) \quad (6)$$

where N is the number of cycles contains in the signal. A signal $x(t)$ is termed second-order cyclostationary if both its first and second-order statistical moments exhibit periodicity with period T_0 for all time t and lag τ . The second-order moment is represented by the autocorrelation function $R_X(t + T_0, \tau) = R_X(t, \tau)$. Assuming the Fourier series expansion

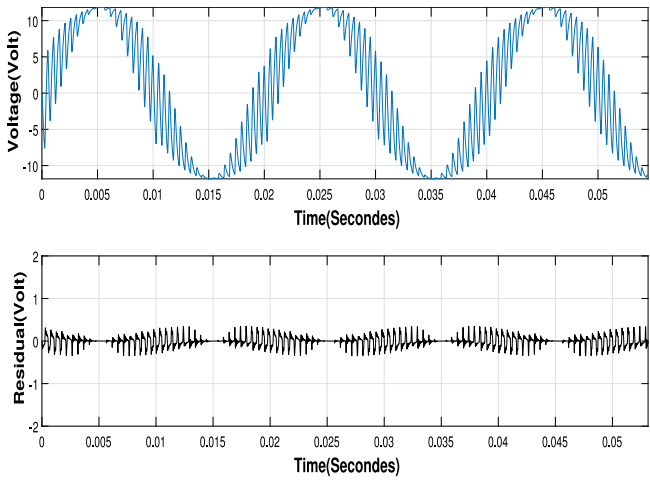


Fig. 12. Voltage and residual for 2 kHz PWM.

of $R_X(t, \tau)$ converges to $R_X(t, \tau)$, the cyclic autocorrelation function is defined as [6]:

$$R_X(t, \tau) = \sum_{n=-\infty}^{+\infty} R_X^{\frac{n}{T_0}}(\tau) e^{j2\pi(\frac{n}{T_0})t} \quad (7)$$

where the Fourier coefficients are:

$$R_X^{\frac{n}{T_0}}(\tau) = \frac{1}{T_0} \int_{-\frac{T_0}{2}}^{+\frac{T_0}{2}} R_X(t, \tau) e^{-j2\pi(\frac{n}{T_0})t} dt \quad (8)$$

The frequencies $\{\frac{n}{T_0}\}_{n \in \mathbb{Z}}$, where n is an integer, are referred to as cycle frequencies. Since the first-order moment induces periodicity in the autocorrelation function, it is necessary to remove this periodicity from the signal to obtain the residual signal prior to autocorrelation computation. In many signal processing applications, analyzing the individual components of a process independently is valuable. These components can often be linked to distinct physical sources. A crucial task involves separating the periodic deterministic and random components of the cyclostationary process. Various techniques exist for isolating the first-order cyclostationary component, including linear prediction [37], envelope analysis [38,39], Self-Adaptive Noise Cancellation (SANC) [37,39,40], cepstral editing [41–43], and time-synchronous averaging (TSA) [39,44].

4.2. Influence of PWM frequency on inverter voltage

To investigate the impact of PWM on the cyclostationary properties of the voltage signal, the signal is decomposed into a first-order cyclostationary (CS1) component and a residual component (CS2). Fig. 12 (blue trace) displays the temporal voltage signal for a PWM frequency of 2 kHz, revealing a clear periodic component and a significant residual signal (noise). The CS1 component is prominently visible in the voltage spectrum (blue panel in Fig. 13), exhibiting two distinct cyclic frequencies. The first peak corresponds to the fundamental voltage frequency ($F_1 = 50$ Hz), while the second peak aligns with the PWM frequency ($F_2 = 2$ kHz). Additionally, sidebands surrounding the PWM cyclic frequency indicate the modulation effect.

4.3. Extraction of residual signal

To isolate the residual signal, a filter was applied to the magnitude of the voltage spectrum. The filter frequency response and impulse response are illustrated in Figs. 14 and 15. Through extensive experimentation, a frequency band of 10 kHz to 12.5 kHz was determined to be optimal for extracting the residual signal, as illustrated by the black trace in Fig. 12.

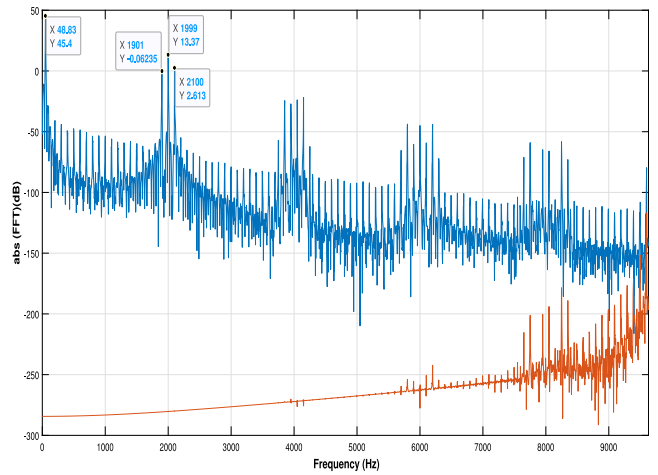


Fig. 13. Spectrum of voltage and residual for PWM frequency of 2 kHz.

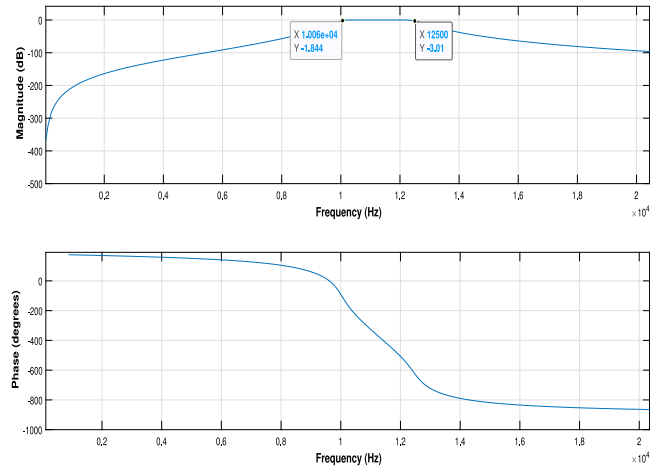


Fig. 14. Frequency response of the filter.

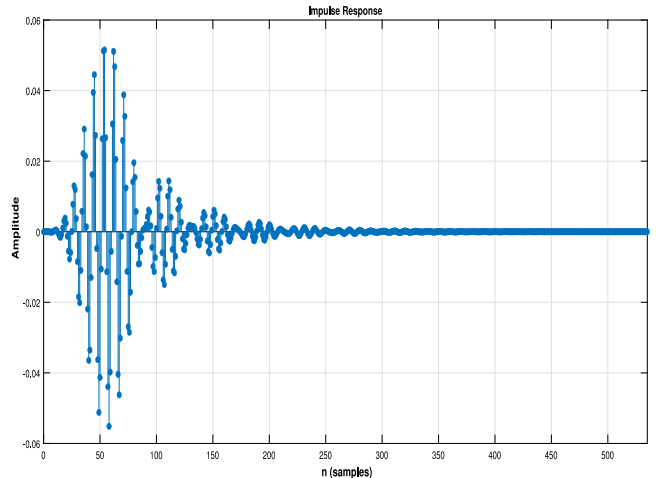


Fig. 15. Impulse response of the filter.

The obtained residual signal is devoid of first-order periodicities (red panel in Fig. 13) as the CS1 component has been eliminated. Nevertheless, this signal may contain components exhibiting periodic power and autocorrelation functions. To reveal potential second-order cyclostationarity, the autocorrelation function is applied to the residual

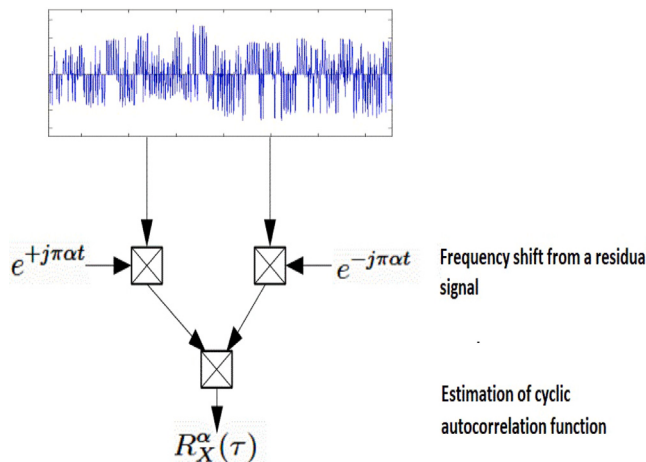


Fig. 16. Estimation of autocorrelation function.

signal. The estimation of the cyclic autocorrelation [45] involves a two-step process outlined in Fig. 16: (i) For a specific cyclic frequency α , the residual signal is frequency-shifted by multiplying it by $e^{+j\pi\alpha t}$ and $e^{-j\pi\alpha t}$, respectively, yielding two new signals. (ii) The correlation of these two signals is computed, resulting in a cross-section of the autocorrelation function at the chosen cyclic frequency α . Figs. 17 and 18 depict the cyclic autocorrelation function and its projection onto the cyclic frequency axis. Two prominent cyclic frequencies are identified at $\alpha_1 = 100$ Hz and $\alpha_2 = 4$ kHz. Notably, the second-order cyclic frequencies are double those of the first-order ($\alpha_1 = 50$ Hz and $\alpha_2 = 2$ kHz). Given the signal's cyclostationarity, the autocorrelation function $R_x(t, \tau)$ exhibits time periodicity, while the cyclic autocorrelation function $R_x^\alpha(\tau)$ is discrete in cyclic frequencies α and continuous in time lag τ .

To investigate the influence of PWM frequency and demonstrate CS properties on voltage signal quality, the voltage frequency is fixed at 50 Hz while the PWM frequency is varied from 1 kHz to 20 kHz in 1 kHz increments. For each PWM frequency, the voltage signal is decomposed into first-order and residual components. Subsequently, two autocorrelation functions are estimated for the residual signal at $\alpha_1 = 100$ Hz and α_2 equal to double the PWM frequency.

To assess the impact of PWM frequency on inverter voltage quality, the first peak of the autocorrelation function projection is considered. For instance, at a PWM frequency of 100 Hz, the first peak occurs at $\alpha_1 = 0.004216$ (Fig. 17(b)) and $\alpha_2 = 0.003967$ (Fig. 18(b)).

Table 2 summarizes the CAF values for each PWM frequency. The results indicate a decreasing residual signal as the PWM frequency increases, with the minimum residual occurring at 20 kHz. Consequently, this PWM frequency is selected for fault detection in the inverter.

Given the cyclostationary nature of the inverter voltage signal, the subsequent section investigates the impact of transistor faults on the voltage signal using this approach.

5. Effect of transistors faults on cyclostationarity

This study focuses on analyzing the residual component of the voltage signal. To investigate the impact of transistor faults on cyclostationary properties, various test cases were conducted, as summarized in Tables 4 and 5. The CAF of faulty voltage signals was compared to that of a fault-free reference signal. Transistors were simulated in two failure modes: open circuit (OC) and short circuit (SC). Initialization parameters of the cyclostationary algorithm are presented in Tab. 3.

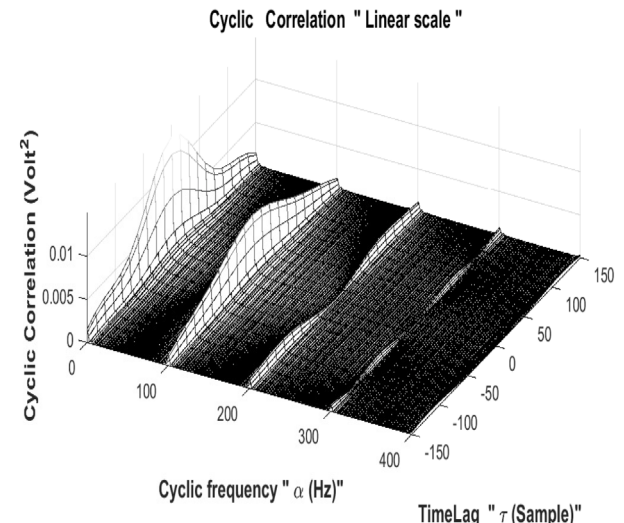
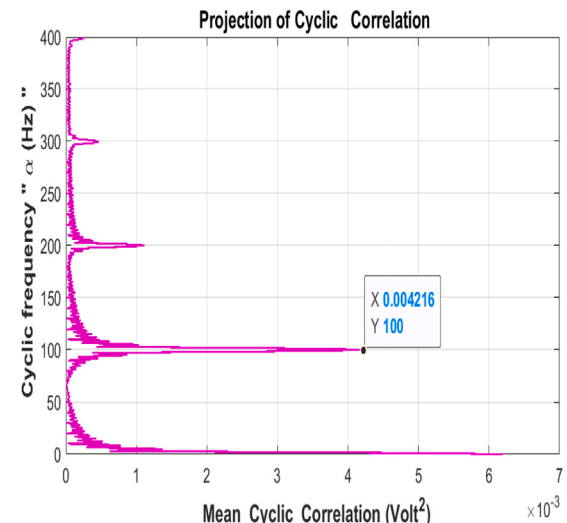
(a) Autocorrelation for $\alpha=100\text{Hz}$ (b) Projection of autocorrelation for $\alpha=100\text{Hz}$

Fig. 17. Magnitude of the cyclic autocorrelation function.

5.1. Open circuit (OC) transistor faults

When SC1 and SC4 were open-circuited, Fig. 19 revealed a series of negative peaks spaced at 0.02 s (50 Hz). A similar pattern, but with positive peaks, was observed when SC2 and SC3 were open-circuited (Fig. 20). These peak sequences were clearly evident in the residual signals (black trace). Additionally, a distortion of the voltage signal was noted. To extract residual signals, the methodology outlined in Section 4.2 was employed to separate first-order (CS1) and second-order (CS2) cyclostationary components from the voltage signal. While these residuals are devoid of CS1, they may exhibit second-order periodicities (CS2). To reveal these hidden periodicities, the CAF was computed for the residual signals at various cyclic frequencies.

The CAF for open-circuit conditions of SC1 (Fig. 23) revealed two cyclic frequencies: $\alpha = 50$ Hz and $\alpha = 100$ Hz. Notably, the PWM cyclic frequency doubled to $\alpha = 40$ kHz in the second-order case compared to the first-order value of $\alpha = 20$ kHz (Fig. 25).

The CAF patterns for open-circuit conditions of SC2, SC3, and SC4 resembled those of SC1, with variations only in the magnitude of the

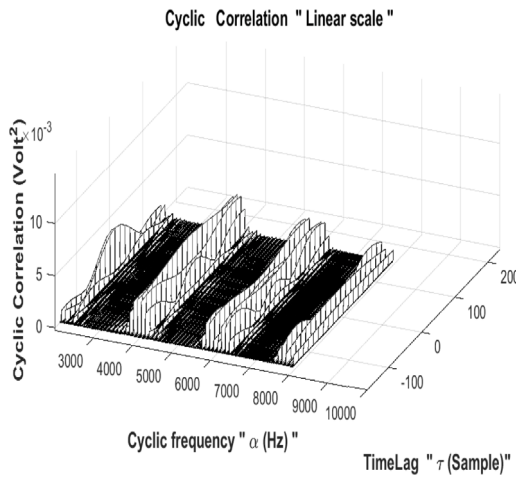
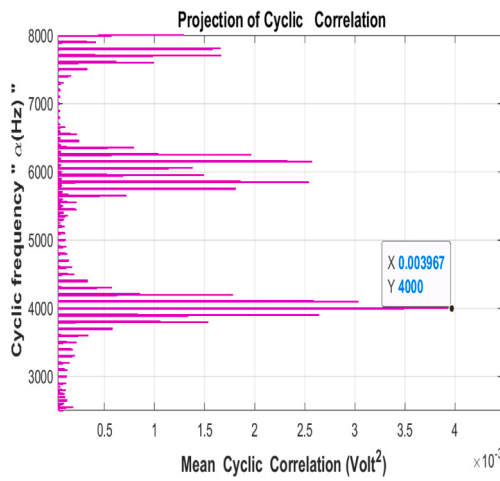
(a) autocorrelation for $\alpha=2\text{KHZ}$ (b) Projection of autocorrelation for $\alpha=2\text{KHZ}$

Fig. 18. Magnitude of the cyclic autocorrelation function.

Table 2

Influence of PWM frequency on cyclostationarity properties of the voltage inverter.

| PWM frequency (kHz) | CAF at 50 Hz | CAF at 20 kHz | RMS |
|---------------------|--------------|---------------|--------|
| 1 | 0.009282 | 0.002418 | 9.2538 |
| 2 | 0.006470 | 0.001674 | 8.6402 |
| 3 | 0.005362 | 0.001668 | 8.4755 |
| 4 | 0.004762 | 0.001597 | 8.4170 |
| 5 | 0.004216 | 0.001466 | 8.3926 |
| 6 | 0.003734 | 0.001237 | 8.3802 |
| 7 | 0.003412 | 0.001222 | 8.3779 |
| 8 | 0.003289 | 0.0009885 | 8.3724 |
| 9 | 0.003272 | 0.0008831 | 8.3708 |
| 10 | 0.002975 | 0.0006705 | 8.3698 |
| 11 | 0.002949 | 0.0005186 | 8.3695 |
| 12 | 0.002259 | 0.0005127 | 8.3694 |
| 13 | 0.000947 | 0.0004433 | 8.3692 |
| 14 | 0.000623 | 0.000318 | 8.3690 |
| 15 | 0.0004658 | 0.0002025 | 8.3684 |
| 16 | 0.0002448 | 0.0001445 | 8.3682 |
| 17 | 0.0001323 | 0.0001095 | 8.3670 |
| 18 | 8.14e-5 | 8.857e-5 | 8.3580 |
| 19 | 5.815e-5 | 7.315e-5 | 8.3545 |
| 20 | 4.793e-5 | 6.185e-5 | 8.3501 |

Table 3

Initialization parameters of the cyclostationary algorithm.

| CS parameter | initialization |
|----------------------------------|---|
| Fundamental voltage frequency | $\alpha_1 = 50 \text{ Hz}$ |
| PWM Frequency | $\alpha_2 = 20 \text{ kHz}$ |
| Second-order cyclic frequency | $\alpha_3 = 40 \text{ Hz}, 50 \text{ Hz}, 100 \text{ Hz}$ |
| Band-pass filter frequency range | 10 kHz–12.5 kHz |

Table 4

CS fault indicators for OC condition.

| | CAF at 50 Hz | CAF at 40 kHz | RMS |
|-----------|--------------|---------------|--------|
| Reference | 3.29e-5 | 1.11e-5 | 8.3701 |
| SC1 OC | 294.40e-5 | 8.035e-5 | 0.8816 |
| SC2 OC | 313.90e-5 | 9.02e-5 | 0.8855 |
| SC3 OC | 313.90e-5 | 9.02e-5 | 0.8855 |
| SC4 OC | 294.30e-5 | 8.035e-5 | 0.8816 |

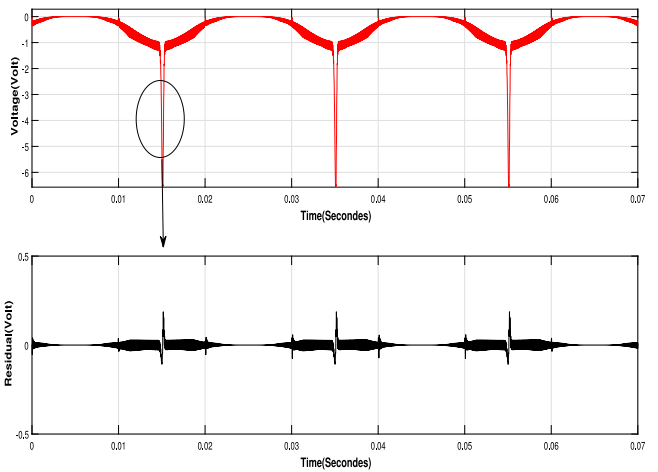


Fig. 19. Voltage when SC1 or SC4 is in open circuit.

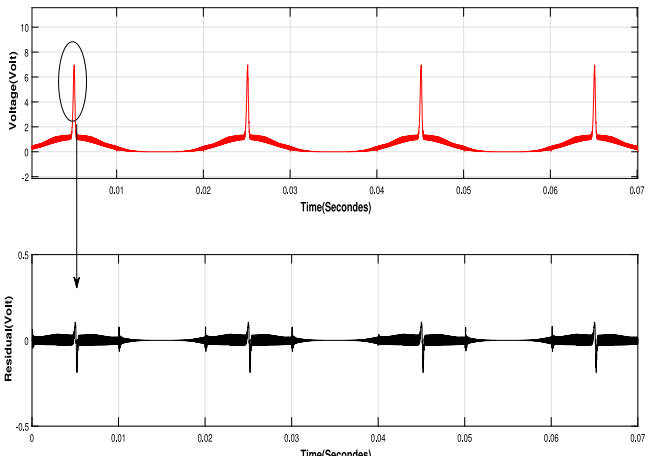


Fig. 20. Voltage when SC2 or SC3 is in open circuit.

CAF at specific cyclic frequencies (Table 4). The cyclic frequencies for open-circuit conditions of SC2, SC3, and SC4 matched that of SC1 (50 Hz).

5.2. Short circuit (SC) transistor faults

Figs. 21 and 22 illustrate voltage signals for short-circuited SC1, SC4 and SC2, SC3, respectively. In the former case, a series of smaller positive peaks with a 0.01-second (100 Hz) spacing was observed, while

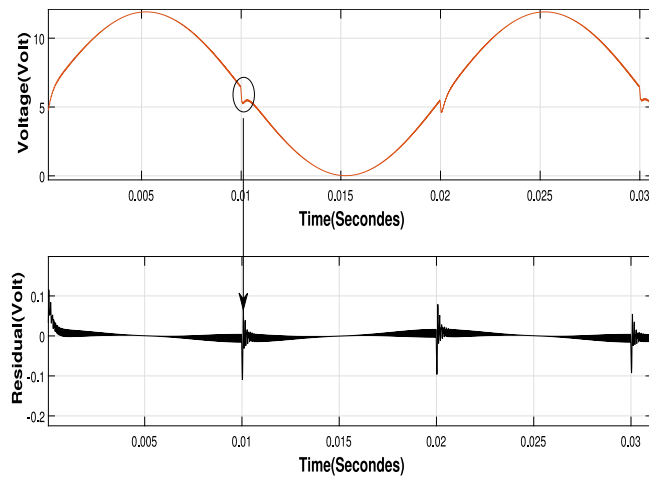


Fig. 21. Voltage when SC1 or SC4 is in short circuit.

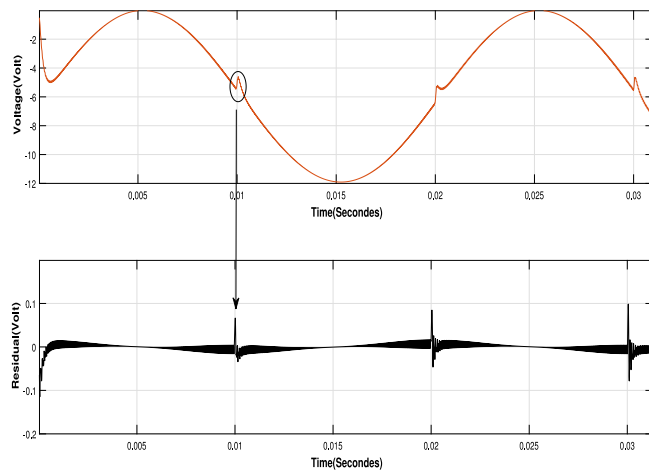
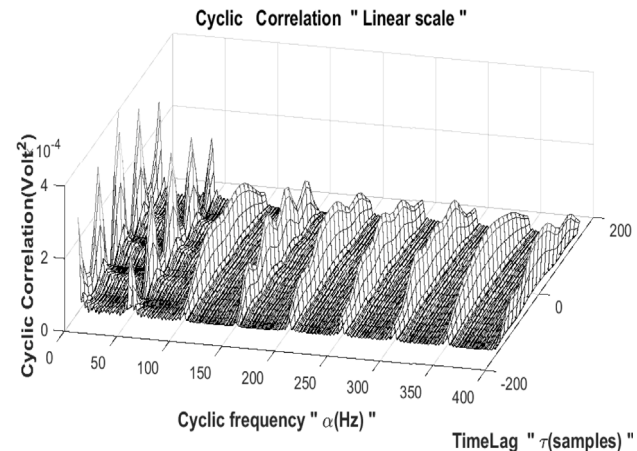
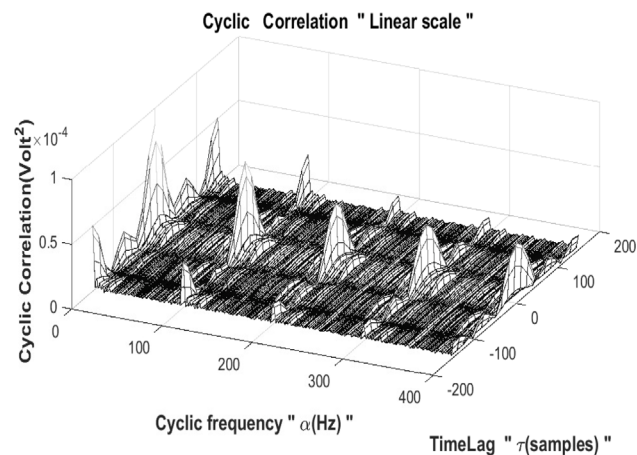
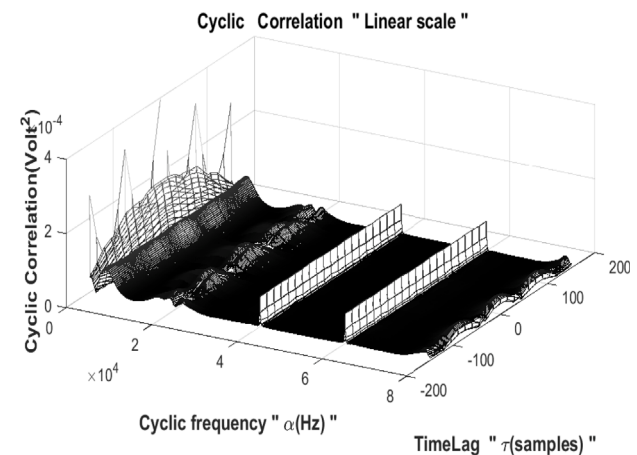


Fig. 22. Voltage when SC2 or SC3 is in short circuit.

Table 5
CS fault indicators for SC condition.

| | CAF at 100 Hz | CAF at 40kHz | RMS |
|--------|---------------|--------------|--------|
| SC1 SC | 7.131e-5 | 0.970e-5 | 7.2770 |
| SC2 SC | 6.804e-5 | 0.968e-5 | 7.2766 |
| SC3 SC | 6.804e-5 | 0.690e-5 | 7.2766 |
| SC4 SC | 7.131e-5 | 0.970e-5 | 7.2770 |

the latter exhibited negative peaks at the same frequency. These peak patterns were also apparent in the corresponding residual signals (black trace). The CAF for short-circuit conditions of SC1 (Fig. 24) revealed cyclic frequencies at $\alpha = 50$ Hz and $\alpha = 100$ Hz. Similar to the open-circuit case, the PWM cyclic frequency doubled to $\alpha = 40$ kHz in the second-order case (Fig. 25). The CAF patterns for short-circuit conditions of SC2, SC3, and SC4 resembled those of SC1, with variations only in the magnitude of the CAF at specific cyclic frequencies (Table 5). The cyclic frequencies for short-circuit conditions of SC2, SC3, and SC4 matched that of SC1 (100 Hz). The results from both open-circuit and short-circuit fault scenarios are summarized in Tables 4 and 5. These tables highlight the CAF values at cyclic frequencies of 50 Hz, 100 Hz, and 40 kHz, as well as the RMS values for each fault condition. The cyclic frequencies for open-circuit faults were consistently 50 Hz, while for short-circuit faults, they were 100 Hz. The CAF magnitude varied depending on the specific fault condition, providing a clear signature for fault detection.

Fig. 23. Cyclic autocorrelation function for $\alpha = 50$ Hz and SC1 OC.Fig. 24. Cyclic autocorrelation function for $\alpha = 100$ Hz and SC1 SC.Fig. 25. Cyclic autocorrelation function for $\alpha = 40$ kHz and SC1 OC.

6. Discussion and comparison

The preceding section detailed various transistor faults within the inverter and demonstrated the cyclostationary nature of the inverter voltage. This section compares fault detection outcomes using both cyclostationary analysis of the residual voltage signal and conventional temporal analysis of the inverter voltage. Temporal analysis offers

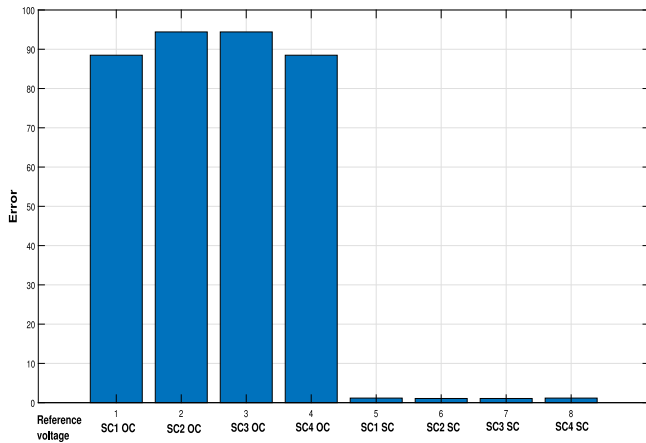


Fig. 26. ΔCAF VS scenarios of transistors faults for cyclic frequencies 50 Hz and 100 Hz.

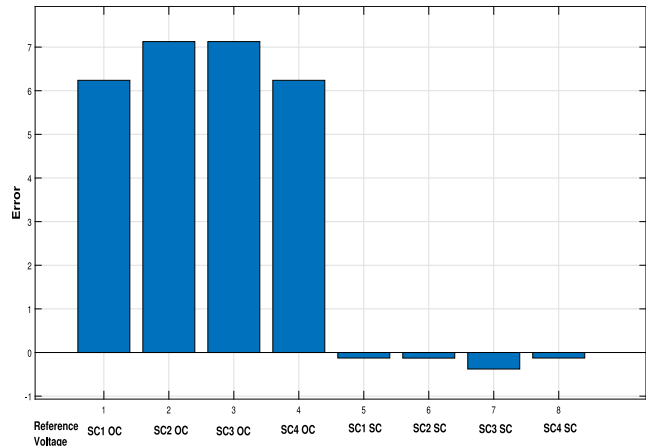


Fig. 27. ΔCAF VS scenarios of transistors faults for cyclic frequency 40 kHz.

advantages in terms of computational efficiency and ease of extracting relevant information from extensive datasets. Indicators such as peak voltage can be employed to capture amplitude trends, although these may be obscured by noise or disturbances. Researchers often favor the root mean square (RMS) value for its sensitivity to operational state variations.

$$RMS = \sqrt{\frac{1}{N} \sum_{k=1}^N (Voltage_k)^2} \quad (9)$$

Cyclostationary (CS) analysis involves decomposing inverter voltage signals into first-order (CS1) and residual components. Employing a methodology similar to Section 4.2, CS fault signatures for various transistor fault types were established (Table 4). Table 4 reveals elevated CS2 values at cyclic frequencies of 50 Hz and 100 Hz for both open-circuit (OC) and short-circuit (SC) transistor faults compared to the reference voltage. Notably, the 40 kHz cyclic frequency exhibits increased CS2 only for OC faults, while decreasing for SC faults. Conversely, the RMS indicator shows a slight decline for all fault conditions.

To quantify indicator sensitivity to faults, an error metric was defined by Eqs. (10) and (11). For instance, with SC1 in OC mode and a cyclic frequency of 50 Hz, the CAF error (ΔCAF) is 88.48, while the RMS error (ΔRMS) is -0.8947. The error results are visualized in Figs. 26, 27, and 28.

$$\Delta CAF = \frac{CAF_{fault} - CAF_{Voltage Reference}}{CAF_{Voltage Reference}} \quad (10)$$

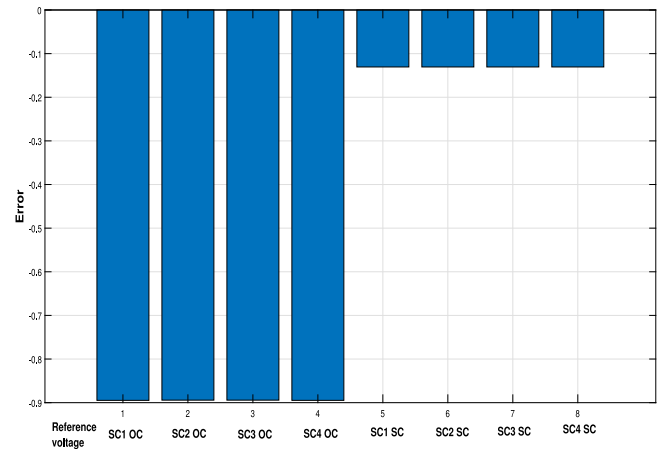


Fig. 28. ΔRMS VS scenarios of transistors faults.

$$\Delta RMS = \frac{RMS_{fault} - RMS_{Voltage Reference}}{RMS_{Voltage Reference}} \quad (11)$$

Analysis of these figures indicates that CS2 is the most sensitive indicator, exhibiting the largest variations for most fault scenarios compared to RMS.

7. Conclusion

In this paper, we investigated the modeling of PV panels under diverse weather conditions and shading scenarios. The Bishop model was adopted due to its effectiveness in representing PV cell behavior in the negative I-V region induced by shading. To address the model's nonlinearity, the Newton-Raphson method was employed to solve the Bishop equation iteratively. A full-bridge inverter was implemented to convert the DC output of PV panels into AC voltage suitable for various loads. The inverter's components, particularly transistors, are susceptible to faults. This study focused on analyzing the impact of transistor faults on inverter performance.

The cyclostationary nature of the inverter voltage signal was exploited to extract fault signatures. By decomposing the signal into periodic and residual components, the cyclic autocorrelation function was employed as a fault indicator. A comparison of signal processing tools was conducted to identify the most fault-sensitive method. By contrasting cyclostationary and root mean square (RMS) analyses, we determined that the cyclic autocorrelation function (CAF) of ripple voltages is the most effective fault indicator. It exhibits the most pronounced drop in the majority of fault scenarios. Additionally, unlike RMS, cyclostationary analysis enables the separate examination of different voltage components (CS1 and CS2).

In this study, validation of cyclostationary analysis was primarily conducted using simulated and benchmark datasets. This approach allowed for a systematic evaluation of the proposed method under a wide range of controlled fault conditions, serving as a critical first step in establishing its theoretical foundation and assessing its performance. While these results provide promising insights into the method's potential, we acknowledge that real-world validation is essential to demonstrate its practical effectiveness comprehensively.

As part of our ongoing and future work, we are actively developing an experimental PV inverter test bench to implement and validate the proposed approach under real-world operating conditions. This will enable us to assess the method's robustness and reliability in practical scenarios.

Future research will also incorporate a boost converter and an MPPT controller, expand the analysis to include various PV panel mismatch scenarios, and generalize the cyclostationary (CS) approach for fault

detection across a broader range of PV system components, including different inverter types and motor drives. Additionally, we plan to extend the application of cyclostationary analysis to fault detection in three-phase inverters, a critical research area with significant implications for renewable energy systems, electric vehicles, and industrial motor drives. In three-phase systems, the voltage and current signals could exhibit more complex cyclostationary properties due to the interaction between the phases. However, the fundamental approach of decomposing the signal into periodic and residual components and analyzing the cyclic autocorrelation function (CAF) could still be applied. The key would be to adapt the analysis to account for the additional frequencies and harmonics present in three-phase systems.

Furthermore, we aim to explore the role of MPPT and DC–DC converters in greater depth. Specifically, we plan to: (i) investigate the impact of MPPT on the inverter's voltage and current signals, particularly under fault conditions, and (ii) examine the interaction between the DC–DC converter and the inverter to understand how faults propagate through the system.

This future research will enhance the model's realism and further validate the proposed fault detection approach within a more comprehensive PV system framework.

CRediT authorship contribution statement

Mohammed Telidjane: Writing – review & editing, Writing – original draft, Validation, Software, Investigation, Formal analysis, Conceptualization. **Benaoumeur Bakhti:** Writing – review & editing, Writing – original draft, Visualization, Validation, Supervision, Project administration, Formal analysis.

Declaration of competing interest

The authors declare that they have no known competing financial interests or personal relationships that could have appeared to influence the work reported in this paper.

Data availability

Data availability is not applicable to this article.

References

- [1] A. Sayigh, Photovoltaics for Sustainable Electricity and Buildings, Springer, 2016, pp. 1–186.
- [2] K. Sundaram, S. Padmanaban, J. Holm-Nielsen, P. Pandiyan, Photovoltaic Systems: Artificial Intelligence-based Fault Diagnosis and Predictive Maintenance, CRC Press, 2022.
- [3] L.D. Jathar, S. Ganeshan, U. Awasarmol, K. Nikam, K. Shahapurkar, M.E.M. Soudagar, H. Fayaz, A.S. El-Shafay, M.A. Kalam, S. Bouadila, S. Baddadi, V. Tirth, A. Nizami, S.S. Lam, M. Rehan, Comprehensive review of environmental factors influencing the performance of photovoltaic panels: Concern over emissions at various phases throughout the lifecycle, Environ. Pollut. 326 (2023) 121474.
- [4] M. Bošnjaković, R. Santa, Z. Crnac, T. Bošnjaković, Environmental impact of PV power systems, Sustainability 15 (15) (2023).
- [5] M. Aghaei, A. Fairbrother, A. Gok, S. Ahmad, S. Kazim, K. Lobato, G. Oreski, A. Reinders, J. Schmitz, M. Theelen, P. Yilmaz, J. Kettle, Review of degradation and failure phenomena in photovoltaic modules, Renew. Sustain. Energy Rev. 159 (2022) 112160.
- [6] B. Long-Dong, Y.-K. Wu, M.-H. Pham, Fault identification and diagnosis methods for photovoltaic system: A review, in: 2021 7th International Conference on Applied System Innovation, ICASI, 2021, pp. 126–129.
- [7] Y.-Y. Hong, R.A. Pula, Methods of photovoltaic fault detection and classification: A review, Energy Rep. 8 (2022) 5898–5929.
- [8] A.F. Amiri, S. Kichou, H. Oudira, A. Chouder, S. Silvestre, Fault detection and diagnosis of a photovoltaic system based on deep learning using the combination of a Convolutional Neural Network (CNN) and Bidirectional Gated Recurrent Unit (bi-GRU), Sustainability 16 (3) (2024).
- [9] A. Abubakar, M.M. Jibril, C.F.M. Almeida, M. Gemignani, M.N. Yahya, S.I. Abba, A novel hybrid optimization approach for fault detection in photovoltaic arrays and inverters using AI and statistical learning techniques: A focus on sustainable environment, Processes 11 (9) (2023).
- [10] G.R. Venkatakrishnan, R. Rengaraj, S. Tamilveli, J. Harshini, A. Sahoo, C.A. Saleel, M. Abbas, E. Cuce, C. Jazlyn, S. Shaik, P.M. Cuce, S. Riffat, Detection, location, and diagnosis of different faults in large solar PV system—a review, Int. J. Low-Carbon Technol. 18 (2023) 659–674.
- [11] A. Mellit, G. Tina, S. Kalogirou, Fault detection and diagnosis methods for photovoltaic systems: A review, Renew. Sustain. Energy Rev. 91 (2018) 1–17.
- [12] T. Sun, C. Chen, S. Wang, B. Zhang, Y. Fu, J. Li, Inverter open circuit fault diagnosis based on residual performance evaluation, IET Power Electron. 16 (15) (2023) 2560–2576.
- [13] K. Osmani, A. Haddad, T. Lemenand, B. Castanier, M. Alkhedher, M. Ramadan, A critical review of PV systems' faults with the relevant detection methods, Energy Nexus 12 (2023) 100257.
- [14] R.B. Pachori, Time-Frequency Analysis Techniques and their Applications, CRC Press, 2023.
- [15] i. Kim, On-line fault detection algorithm of a photovoltaic system using wavelet transform, Sol. Energy 126 (2016) 137–145.
- [16] B. Taghezouit, F. Harrou, Y. Sun, W. Merrouche, Model-based fault detection in photovoltaic systems: A comprehensive review and avenues for enhancement, Results Eng. 21 (2024) 101835.
- [17] G.M. El-Banby, N.M.M.B.A. Abouzalm, W.F.A.E.A. Ramadan, Photovoltaic system fault detection techniques: a review, Neural Comput. Appl. 35 (2023) 24829.
- [18] L. Costa, A. Silva, R.J. Bessa, R.E. Araújo, PV inverter fault classification using machine learning and clarke transformation, in: 2023 IEEE Belgrade PowerTech, 2023, pp. 1–6.
- [19] C. Drif, A. Soualhi, H. Nouri, Diagnosis and detection of open-circuit faults in inverters using principal component analysis and neural networks, in: 2024 2nd International Conference on Electrical Engineering and Automatic Control, ICEEAC, 2024, pp. 1–6.
- [20] V.S.B. Kurukuru, A. Haque, M.A. Khan, S. Sahoo, A. Malik, F. Blaabjerg, A review on artificial intelligence applications for grid-connected solar photovoltaic systems, Energies 14 (15) (2021).
- [21] B. Li, C. Delpha, D. Diallo, A. Migan-Dubois, Application of artificial neural networks to photovoltaic fault detection and diagnosis: A review, Renew. Sustain. Energy Rev. 138 (2021) 110512.
- [22] H.B. Tian Lisi, Y. Qiang, Fault diagnosis of three-level inverter based on convolutional neural network and support vector machine, J. Chin. in. Eng. 46 (8) (2023) 829–838.
- [23] W.A. Gardner, Cyclostationarity in Communications and Signal Processing, IEEE Press, New York, 1994, p. 504.
- [24] F. Perez-Sanjines, C. Peeters, T. Verstraeten, J. Antoni, A. Nowé, J. Helsen, Fleet-based early fault detection of wind turbine gearboxes using physics-informed deep learning based on cyclic spectral coherence, Mech. Syst. Signal Process. 185 (2023) 109760.
- [25] M. Telidjane, Modélisation Des Panneaux Photovoltaïques Et Adaptation De La Cyclostationnarité Pour Le Diagnostic (Ph.D. thesis), Université de Lyon, 2017, p. 133.
- [26] M. Telidjane, B. Bakhti, Enhanced estimation of seasonal irradiance patterns: the adapted time synchronous average method, Submitted for publication.
- [27] I. Mayergoyz, S. Tyagi, Pulse Width Modulation In Power Electronics, World Scientific Publishing Company, 2021.
- [28] A. Aktaş, Y. Kirçicek, Chapter 8 - solar hybrid systems for smart grids, in: A.A. s, Y.K. cicek (Eds.), Solar Hybrid Systems, Academic Press, 2021, pp. 153–178.
- [29] L. Ashok Kumar, S. Albert Alexander, M. Rajendran, Chapter 1 - inverter topologies for solar PV, in: L. shok Kumar, S. Albert Alexander, M. Rajendran (Eds.), Power Electronic Converters for Solar Photovoltaic Systems, Academic Press, 2021, pp. 1–39.
- [30] J. Bishop, Computer simulation of the effects of electrical mismatches in photovoltaic cell interconnection circuits, Sol. Cells 25 (1988) 73–89.
- [31] M. Alonso-García, J. Ruiz, W. Herrmann, Computer simulation of shading effects in photovoltaic arrays, Renew. Energy 31 (12) (2006) 1986–1993.
- [32] L. Bun, Détection et Localisation de Défauts pour un Système PV (Ph.D. thesis), Laboratoire G2ELAB Université de Grenoble France, 2011, pp. 1–190.
- [33] S. Silvestre, A. Boronat, A. Chouder, Study of bypass diodes configuration on PV modules, Appl. Energy 86 (9) (2009) 1632–1640.
- [34] E. Karatepe, M. Boztepe, M. Çolak, Development of a suitable model for characterizing photovoltaic arrays with shaded solar cells, Sol. Energy 81 (8) (2007) 977–992.
- [35] V. Salas, E. Olías, A. Barrado, A. Lázaro, Review of the maximum power point tracking algorithms for stand-alone photovoltaic systems, Sol. Energy Mater. Sol. Cells 90 (11) (2006) 1555–1578.
- [36] K. Ishaque, Z. Salam, H. Taheri, Modeling and simulation of photovoltaic (PV) system during partial shading based on a two-diode model, Simul. Model. Pr. Theory 19 (7) (2011) 1613–1626.
- [37] R.B. Randall, N. Sawalhi, M.D. Coats, A comparison of methods for separation of deterministic and random signals, Int. J. Cond. Monit. 1 (2011) 11–19.
- [38] T. Kidar, Diagnostic Des Défauts De Fissures D'engrenages Par L'analyse Cyclostationnaire (Ph.D. thesis), Laboratoire des Signaux et des Processus Industriels (LASPI) Université Jean Monnet St-Etienne, France, 2015, pp. 1–147, arXiv:arXiv: 1011.1669v3.

- [39] F. Bonnardot, Comparaison Entre Les Analyses Angulaire Et Temporelle Des Signaux Vibratoires De Machines Tournantes. Etude Du Concept De Cyclostationnarité Floue (Ph.D. thesis), Institut national polytechnique de Grenoble, 2004, p. 171.
- [40] S. Maiz, Deterministic/cyclostationary signal separation using bootstrap, in: 11th IFAC International Workshop on Adaptation and Learning in Control and Signal Processing, University of Caen Basse-Normandie, Caen, France, July 3-5, 2013 ThS6T4.4, 2013, pp. 641–646.
- [41] M. El Badaoui, Contribution au Diagnostic Vibratoire des Réducteurs Complexes à Engrenages par l'Analyse Cepstrale (Ph.D. thesis), Université Jean Monnet St-Etienne, France, 1999.
- [42] C. Peeters, P. Guillaume, J. Helsen, A comparison of cepstral editing methods as signal pre-processing techniques for vibration-based bearing fault detection, *Mech. Sys. Signal Process.* 91 (2017) 354–381.
- [43] R.B. Randall, N. Sawalhi, A new method for separating discrete components from a signal, *Sound Vib.* 45 (2011) 6–9.
- [44] E. Bechhoefer, M. Kingsley, A review of time synchronous average algorithms, *Annu. Conf. Progn. Heal. Manag. Soc.* (2009) 1–10.
- [45] S. Maiz, Estimation Et Détection Des Signaux Cyclostationnaires Par Les Méthodes De Re-Echantillonage Statistique :Applications À L'analyse Des Signaux Biomécaniques (Ph.D. thesis), Laboratoire des Signaux et des Processus Industriels (LASPI) Université Jean Monnet St-Etienne, France, 2014.